Mechanical behaviour of ductile polymer cellular model structures manufactured by FDM

Jacopo Agnelli[a], Claudia Pagano[b], Irene Fassi[b], Laura Treccani[c], Fabio Bignotti[a], Francesco Baldi[a,*]

[a] *Università degli Studi di Brescia, Dipartimento di Ingegneria Meccanica e Industriale, Via Branze 38, I - 25123 Brescia, Italy*
[b] *STIIMA-CNR, Institute of Intelligent Industrial Systems and Technologies for Advanced Manufacturing, Consiglio Nazionale delle Ricerche, Via A. Corti 12, I - 20133 Milano, Italy*
[c] *CSMT Gestione S.c.a.r.l., Via Branze 45, I - 25123 Brescia, Italy*

Abstract

In this work, Acrylonitrile-Butadiene-Styrene model structures were manufactured by FDM, and their mechanical behaviour investigated under compression, both at small and at large strains. The structure design strategy adopted, based on the use of circular cross-section beam-like elements formed under controlled conditions, led to obtain open-celled structures (with a porosity degree of $\approx$ 65%) composed of unit cells with different shapes and dimensions assembled to form regularly repeating patterns. The stress-strain behaviour, from cube- and prism-shaped specimens with different sizes and loaded along different directions, was discussed in the light of the outcomes from (i) cyclic compression experiments and (ii) morphological analyses of cryogenic fracture surfaces of specimens compressed at high strain levels. The response along the 3D-stacking direction was traced back to the elastic-plastic case, with non-recoverable strain starting to accumulate between 3% and 5% strain and structure densification starting below 20%. The specimen size effects turned out to be not dominant, even if slightly higher levels of stiffness and strength were measured for the largest cube. This result was discussed on the basis of the peculiar morphology of the structure examined.

*Corresponding author
Email address: francesco.baldi@unibs.it (Francesco Baldi)

Keywords: ABS; additive manufacturing; FDM; mechanics of cellular solids; compression tests; cyclic tests

1. Introduction

Additive manufacturing (AM) shows good capability for the fabrication of parts of almost any shape in a very short time allowing designers and engineers to tailor the products to the customers' requirements. Among the additive manufacturing processes, fused deposition modelling (FDM) has become popular due to the low cost and large range of usable materials (Penumakala et al., 2020). In FDM of polymeric materials, a filament is heated and then deposited layer-by-layer from a nozzle on a platform according to the part model, which is sliced into several 2D layers to obtain the tool path motion of the nozzle. It was initially dedicated to prototypes, but thanks to recent technological advancements, nowadays it is used to print parts for industrial applications in a lot of sectors. In the aerospace and automobile industry, FDM manufactured parts are used to replace traditional metal components and reduce their weight maintaining appropriate robustness, this also reduces the turnaround time for part repair. Electronic applications take advantage of the development of polymer composites with tailored electrical properties to manufacture FDM parts for dielectric, conductive, sensors and energy storage applications. In biomedical applications (Javaid and Haleem, 2018), one of the greatest advantages of AM is the straightforward process chain from diagnosis to surgery, using the same imaging and scanning results, necessary for the diagnosis, to create the digital design of the physical model. In this way, reverse engineering allows the manufacturing of highly customizable products. In tissue engineering, FDM allows the fabrication of complex internal architecture in scaffolds with controlled porosity and interconnected network. It is suitable for the manufacturing of polymer cellular structures, ensuring the possibility to obtain high shape complexity and size flexibility, while guaranteeing structural regularity and repeatability thanks to the controlled filament deposition and thermo-mechanical history imposed. Sev-

eral recent works have been focused on lattice structures manufactured by AM. They can be considered as metamaterials since they can show physical properties absent in the constituent materials and originated from the architecture (Askari et al., 2020).

This work is part of a larger research activity aimed at developing new fracture mechanics testing methodologies for the characterization of elastic-plastic open-celled cellular solids with a moderately high mechanical compliance (elastic modulus in the range 10÷100 MPa) and characterized by a pronounced degree of structural heterogeneity (Gibson and Ashby, 1997). In this framework, the FDM technology was exploited to manufacture model structures to be used as reference testing systems in addressing specific fundamental and methodological issues. In the present paper, the mechanical behaviour of these model structures was investigated both at small and at large strains, and accompanied by morphological analyses, with the aim of laying the foundations for the study of their structural integrity. Three-dimensional open-celled structures in a ductile polymer (Acrylonitrile-Butadiene-Styrene, ABS), composed of unit cells with different shapes and dimensions and assembled to form regularly repeating patterns, were examined. The design of the structure was based on circular cross-section beam-like elements, directly formed by the filament extruded by the 3D printer under controlled conditions. Similar design strategies can be found in literature ((Zhou et al., 2016), (Shalchy et al., 2020), (Bachtiar et al., 2021)). This approach is inherently different from the most widely employed in FDM literature, where the nozzle deposits consecutive filament portions that stack to form the walls/struts of the cells ((Platek et al., 2020), (Kumar et al., 2022), (Wang et al., 2023)).

The stress-strain behaviour of the manufactured 3D-structures was studied by means of monotonic compression tests carried out in quasi-static conditions on cube- and prism-shaped specimens; the effects of the specimen size, as well as of the test loading direction, were investigated. Cyclic loading-unloading compression tests were also carried out to study, on a global scale, the non-recoverable strain accumulation processes in the elastic-to-plastic transition

phase. The effects of the accumulated plastic deformation on the material structure were also investigated locally, analyzing the deformed structures at large applied strains (between 20% and 60%), to elucidate the mechanisms governing the 3D-structure deformation. Further, the mechanical behaviour of the polymeric element forming the 3D-structures, which is the filament extruded through the 3D printer nozzle, was investigated by means of uniaxial tensile tests carried out on portions of the filament produced with the same process conditions used for the manufacturing of the structures.

2. Experimental

2.1. Material and fabrication of the structures

An Original Prusa i3 MK3S+ FDM printer, equipped with a nozzle of 0.4 mm in diameter, was used to manufacture the model structures with a commercial filament of ABS. Special attention was paid to the preliminary design phase, in terms of both selection of the appropriate process conditions and of the suitable architectures of the specimens. The nozzle and plate temperatures were set at 220°C and 80°C, respectively, and the material was extruded at 400 mm/min, corresponding to an apparent shear rate at the nozzle die (Macosko, 1994) of 133 s^{-1}. Such value, typical of a standard die forming process, suggests that a given (non-null) degree of macromolecular pre-orientation is present in the material in the extruded filament. The glass transition temperature of the polymer in the extruded filament was measured by Differential Scanning Calorimetry (by means of a TA Instruments calorimeter, model Q100, with a scanning heating rate of 10°C/min, under a nitrogen atmosphere, on samples collected from the 3D-printed structures) and it resulted of 104°C. The density of the extruded filament, ρ_{ABS}, was determined from independent measurements of mass and volume carried out on several portions of the filament printed with the same process parameters used for the manufacturing of the 3D-structures, and it resulted of 1.06 $\pm$ 0.02 g/cm^3. For each filament portion examined, the mass was measured with a digital analytical balance with 10^{-1} mg resolution, and

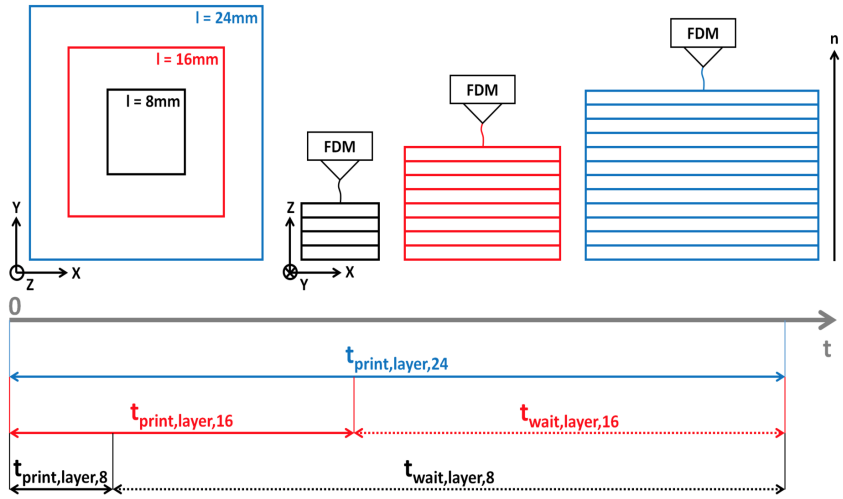

Figure 1: Visual representation of specimen manufacturing process and times (Eq. 1).

the volume calculated from length measurements carried out by means of 1 µm resolution micrometer (for the sample diameter) and by the optical microscope Leica MS5 equipped a travelling xy-table moved by micrometers having the graduation of 1 µm (for the sample length).

The 3D-printed specimens examined were cubes and prisms with square-base, manufactured with a 30% "infill density". This means that the cubes and prisms are not completely solid, which would correspond to 100% "infill density", but are nominally 70% hollow. The specimen base was on the X-Y plane, and the height along the Z direction (see Figure 1). The deposition of a layer - line by line, in the X-Y plane (in-plane deposition) - was followed by the 0.4 mm upward shift of the nozzle (along the Z direction, which is the layer stacking direction) and, by the deposition of the subsequent layer (Figure 1). The process was repeated for all the n layers (Figure 1) of the specimen, where n is a multiple of 4, in order to have a ordered 4-layer basic unit with filament deposition at 0°, 45°, 90° and −45°, in the first, second, third and fourth layer, respectively (see Figure 2). Such basic unit was then repeated in the layer stacking direction (Z) to obtain the specimen prefixed height. In

order to study the effect of the specimen size on the mechanical response under compression, two different specimen shapes were manufactured: (i) cubes with varying side length values (8, 16, 24 mm); (ii) square-base prisms with 16 mm base side length and varying height (8 and 24 mm). The complete recap of the model structures, as well as the convention adopted for their labelling, is presented in Table 1. In a continuous printing process with a fixed material deposition rate, the time necessary to complete the deposition of a single layer varies according to the layer surface area of the specimen: the smaller this area, the lower the time. In the case of the cube-shaped specimens here examined (C_8, C_{16} and C_{24}), a continuous deposition of material would therefore result in different cooling and solidification histories undergone by the polymeric material in the cubes with different base sizes. In order to reduce as much as possible these differences in the thermal histories, for the smaller specimens (C_8 and C_{16}) a specific waiting time was added to the manufacturing time, between the depositions of two consecutive layers. More specifically, the time necessary for the complete manufacturing of a C_{24} layer ($t_{print,layer,24} = 58$ s) was taken as the reference, and for C_8 and C_{16} specimens an appropriate waiting time ($t_{wait,layer,8(16)}$) - when no deposition took place - was introduced at the end of each layer printing phase so that (see also Figure 1):

$$t_{print,layer,8} + t_{wait,layer,8} = t_{print,layer,16} + t_{wait,layer,16} = t_{print,layer,24} \quad (1)$$

2.2. Characterization

2.2.1. Morphological analyses and density measurements

Morphological characterization of the specimens was carried out, at the macro-scale, by means of standard optical and digital microscopy techniques (Leica microscopes, models MS5 and DMS300). These analyses allowed also the assessment of the quality of the samples. Additional morphological analyses were performed on the C_{16} structures after deformation under compression at large strain levels (the compression tests on the 3D-structures are described

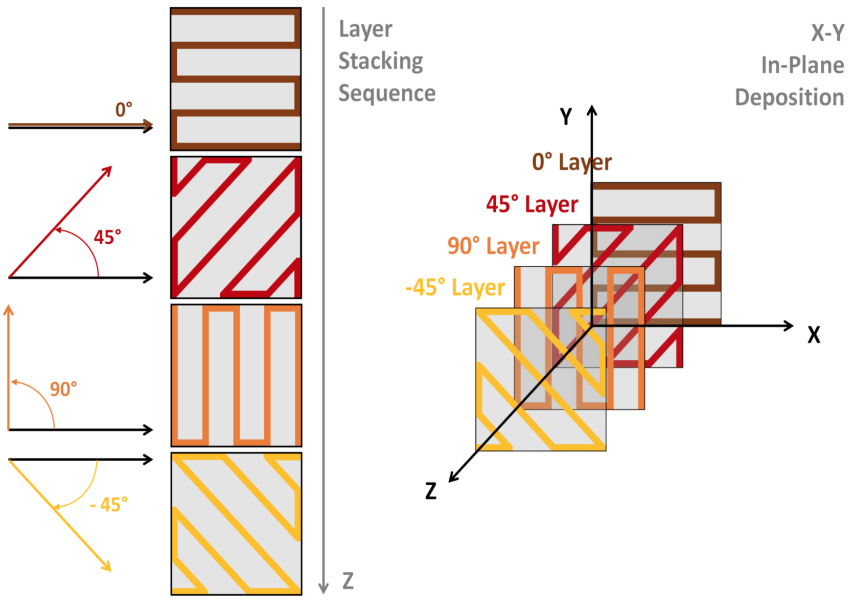

Figure 2: Infographic of the main 4 layers and their sequence in layer stacking direction to form the repeating basic unit for the 3D structures.

below). Three nominal apparent strains, namely 20%, 40% and 60%, were analyzed on three different specimens. For each specimen, the load was rapidly removed once the pre-set level of deformation was reached, and the deformed specimen was then kept at room temperature for at least one week in order to allow most of the free strain recovery. A sharp pre-notch was then introduced at a given position into each of the three deformed specimens and into one undeformed specimen. Each specimen was then brought to complete fracture after a prolonged exposure to liquid nitrogen, in such a way that any plastic deformation associated with the fracture process that started from the tip of the pre-notch could be hindered. The cryogenic-fracture surfaces (parallel to the X-Z plane) of the various specimens was then observed at the microscopes.

For each specimen, the apparent density, $\varrho_{\mathrm{app,3D}}$, was determined as the ratio between the specimen mass and its volume. Mass measurements were carried out by means of a digital analytical balance with 10^{-1} mg resolution. The volume was determined from the specimen dimensions, measured using either

a digital micrometer (with 1 µm resolution) or a Vernier caliper (with 50 µm resolution), for lengths lower or higher than 20 mm, respectively. An "apparent" character is attributed to the density of the specimen in consideration of the porous nature of the material.

2.2.2. Mechanical tests

Tensile tests on the extruded filament. Uniaxial tensile tests were carried out on portions of the filament produced with the same process conditions used for the manufacturing of the 3D-structures. An Instron test system (model 3366) equipped with a 500 N load cell was used, and the tests were performed at room temperature. The testing configuration is showed in Figure 3. A graph paper mask was used in order to make the specimen handling and correct positioning phases easier. The distance between the grips, l_0, was fixed at 70 mm, and the crosshead speed was set at 3.5 mm/min in such a way to obtain a nominal strain rate equal to that used in the compression tests on the 3D-structures (see below, in this Section). Five different samples were tested. For each sample, the load vs crosshead displacement curve was recorded, and then converted into a nominal tensile stress vs nominal tensile strain curve. The stress was determined as the load over the initial sample cross section (the filament diameter was measured as described at Section 2.1); the strain was calculated from the crosshead displacement, divided by l_0.

Compression tests on the 3D-structures. Compression tests were performed by using the Instron test system 3366 equipped with a 10 kN load cell, at room temperature. Both monotonic (one-way) and cyclic compression tests were carried out. In the monotonic tests, the crosshead speed was varied depending on the height of the specimen under analysis, in order to obtain the same apparent compression strain rate, which was 0.05 min^{-1}. A thin layer of paraffin oil was deposited on each compression plate in order to reduce the friction between the specimen and the plate. The testing configuration is showed in Figure 4. The experiments were meant to explore the following effects (with reference to Table 1):

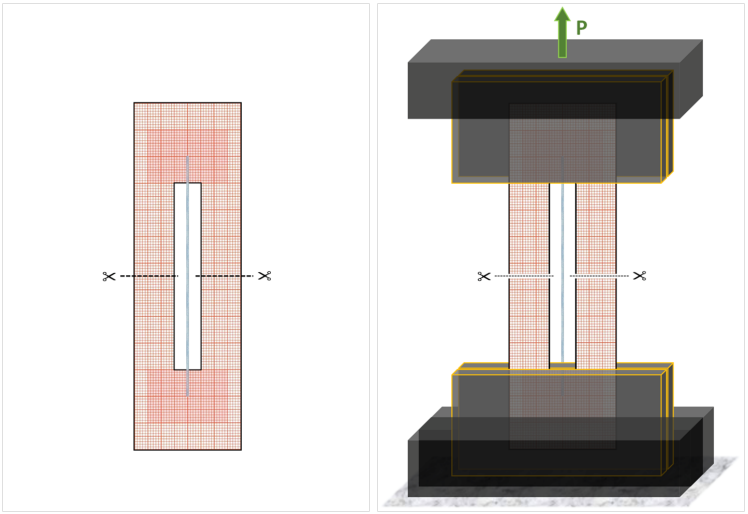

(a) (b)

Figure 3: Tensile test procedure on the extruded filament of ABS. (a) Preparation of the graph paper mask for handling and positioning phases; (b) execution of the test.

- loading direction effect, from tests on C_{16} specimens carried out with the loading direction either parallel or orthogonal to the 3D-growth (Z) direction;
- size effect, from tests on C_8, C_{16} and C_{24} specimens loaded along the Z direction;
- height effect, from tests on P_8, C_{16} and P_{24} specimens loaded along the Z direction.

For each specimen geometry and loading direction examined, four specimens were tested. For each specimen tested, the load, P, vs crosshead displacement, u_r, curve, output of the test, was converted into the apparent stress, σ_{app}, vs apparent strain, ε_{app}, curve. σ_{app} was calculated as P over the initial cross section of the specimen, ε_{app} as the crosshead displacement, u_{cor} - properly corrected to remove the "foot zone" of the P vs u_r curve corresponding to the approaching and plate-specimen contact establishment phases - divided by the

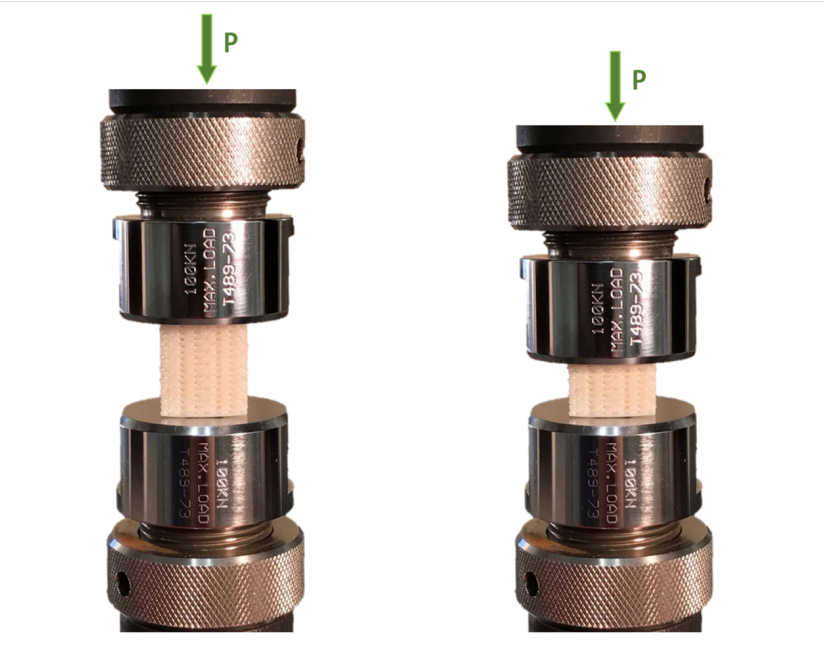

Figure 4: Compression tests on 3D-printed cellular structures.

initial height of the specimen. The dimensions of the specimens were measured as described at Section 2.2.1. The compression stress and strain here determined have been considered "apparent" because of the cellular nature of the systems examined. Tests were interrupted at an ε_{app} level higher than 50%, with the only exception of the experiments on the C_{24} specimens that were interrupted at smaller strains, when the load reached the full-scale of the load cell.

The cyclic compression tests were carried out on the cube-shaped specimens with different side lengths (C_8, C_{16}, C_{24}) - one single specimen for each size. Each cycle consisted of a loading phase, characterized by the same apparent compression strain rate used in the monotonic tests, followed by an unloading phase at a doubled speed. The crosshead displacement, u_r, reached at the end of the loading phase increased from cycle to cycle according to the scheme presented in Figure 5a. Load, P, vs u_r curves were collected as output, and then properly corrected for the "foot zone", as mentioned above, in order to obtain the P vs u_{cor} curve (Figure 5b). The tests were interrupted at $\varepsilon_{app} \approx 25\%$. For

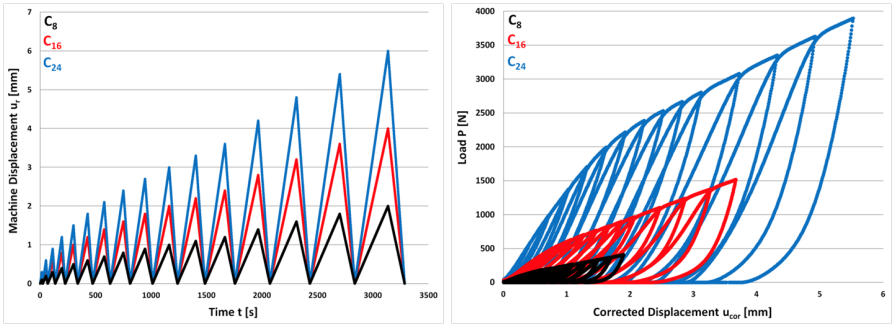

(a) (b)

Figure 5: Cyclic compression tests on cube-shaped C_8, C_{16}, C_{24} specimens. (a) Test input as Machine Displacement, u_r , vs Time, t, plot; (b) output curves expressed in terms of Load, P, vs Corrected Displacement, u_{cor} (see text).

each cycle, the maximum apparent deformation applied, $\varepsilon_{app,max,appl}$, and the residual apparent deformation after the unloading phase, $\varepsilon_{app,res}$, which are regarded as the fundamental quantities for this kind of analysis, were determined. In particular, $\varepsilon_{app,res}$ was taken in correspondence of the last point of monotonic decrease on the unloading curve below the threshold value of 0.5 N.

Table 1: Specimens tested (with indication of geometry, dimensions and loading direction used in the compression tests) and mechanical properties measured under compression (apparent elastic modulus, E_{app}, and apparent stress at failure, $\sigma_{app,failure}$). For each property, the mean value ± standard deviation is reported.

3D-Specimens					
Geometry	Nominal Characteristic Dimension[a] [mm]	Test Loading Direction[b]	Code	E_{app} [MPa]	$\sigma_{app,failure}$ [MPa]
Cube	8	Parallel	C_8	45 ± 4.8	2.4 ± 0.23 [c]
	16	Parallel	C_{16}	39 ± 3.9	2.1 ± 0.12
	16	$Orthogonal_X$	C_{16-X}	71 ± 2.7	3.9 ± 0.47
	16	$Orthogonal_Y$	C_{16-Y}	71 ± 3.9	4.2 ± 0.53
	24	Parallel	C_{24}	54 ± 3.9	3.0 ± 0.29
Prism[d]	8	Parallel	P_8	40 ± 3.5	2.3 ± 0.43
	24	Parallel	P_{24}	40 ± 1.2	1.5 ± 0.13

[a]: for the cube-shaped specimens, the characteristic dimension is the length of the side of the cube; for the prism-shaped specimen, it is the height of the prism, read along the specimen 3D-growth direction according to the layer-to-layer fabrication approach of the FDM technology. [b]: "Parallel" indicates that the specimen loading direction used in the compression tests was parallel to the specimen 3D-growth direction; "Orthogonal" indicates that the loading direction was perpendicular to the specimen 3D-growth direction (subscript "X" or "Y" specifies the loading direction used in the test, see Figure 1 and Figure 8b). [c]: Average of two values, measured on the two specimens with ϱ_{rel} between 0.33 and 0.37 (see section 3.1); uncertainty determined as the semi-dispersion. [d]: Rectangular prism with 16mm-side square base.

3. Results and Discussion

3.1. Morphology and density of the structures

The two-dimensional development of the 3D-structure can be easily detected by looking at the manufactured 3D-specimens along an axis parallel to the 3D-printing growing direction (Z direction). Figure 6a shows the X-Y top surface view of specimens C_{24}, C_{16} and C_8. The 3D-structures appear characterized, on the X-Y plane, by a repetition of figures. Each figure, whose characteristic size is of the order of 1 mm, is generated from the complex overlapping, along the Z direction, of the layers with different orientation. This defines space frames (cells) with different shapes and dimensions. Figures and cells can be seen also from the sectional view of the structure that is reported in Figure 6b, obtained from a CAD model from the relief of the C_8 specimen. The cells are fully interconnected, and they even give rise to corridors along the entire height of the specimen.

The structure of the 8mm-side specimen (C_8) can be regarded as the fundamental building block to perform a morphological analysis of the specimens with different sizes. As shown in Figure 6a, the C_8 structure can be found right in the centre of the C_{16} structure, which in turn can be found right in the centre of the C_{24} structure. Further, C_{24} shows C_8 structures at its corners, embedded in incomplete C_{16} structures. These latter (i) overlap partially the central C_{16} structure in co-shared regions, and (ii) are mutually joined by connecting zones. These observations suggest that these lattice structures could be regarded, at the macro-scale, as a form of cellular solids characterized by a regular repetition of a basic pattern - C_8 and its supersets - formed by cells with different shapes and sizes. The degree of structural heterogeneity, ensured by such design strategy, effectively turned out to be higher than that commonly observed in the literature on FDM structures (see, for example, (Maskery et al., 2018), (Abou-ali and Al-ketan, 2019), (Ling et al., 2019), (Eren et al., 2022)).

The key parameter that characterizes the structures is their apparent density, $\rho_{app,3D}$. From classical literature on cellular solids (Gibson and Ashby, 1997),

the most widely employed specimen-related parameter is the relative density, $\rho_{rel,3D}$, which is the ratio between $\rho_{app,3D}$ and the material density, which in the case of the structures here examined is the density of the filament extruded from the 3D-printer, ρ_{ABS}. As expected by considering that the various specimens were ideally identical from the structural point of view, the differences recorded among their $\rho_{rel,3D}$ values were very small. A 3.2% standard deviation was obtained with a $\rho_{rel,3D}$ mean value of 0.35. It is worth noting that, according to (Gibson and Ashby, 1997), such a value of $\rho_{rel,3D}$ is typical of structures that are on the border between "true cellular solids" (with relative density smaller than 0.3) and "solids containing isolated pores". In order to rely on a more homogeneous base of data, the specimens with a value of $\rho_{rel,3D}$ outside 0.35 ± 0.02 were not considered in the analysis . This is the case of only two specimens belonging to the C_8 series.

3.2. Mechanical behaviour

Under uniaxial tension, the extruded filament of ABS exhibited a typical ductile behaviour, as shown by the nominal tensile stress vs nominal tensile strain curve in Figure 7. The material showed yielding at a strain level of $\approx$ 3%, and reached breakage at a strain level close to 35%. From the stress-strain curves obtained for the five different samples examined, the mechanical stiffness (Young's modulus, E_{ABS}) and strength (tensile stress at yield, $\sigma_{y,t,ABS}$) of the material were determined. E_{ABS}, evaluated from the slope of the curve in the initial linear region, resulted of 1910 ± 110 MPa (mean value $\pm$ standard deviation); $\sigma_{y,t,ABS}$, taken at the peak of the curve, resulted of 36.2 ± 2.6 MPa. On the macro-scale, strain localization phenomena characterized by a progressive development of whitened zones along the deformed strand (see Figure 7) were noticed during the test, just after yielding. These whitened zones should be directly related, on the micro-scale, with the deformation mechanism of voiding (rubber particle cavitation and multiple crazing (Agnelli et al., 2018)). By increasing the applied strain, the whitened zones tend to coalesce up to the breakage of the strand.

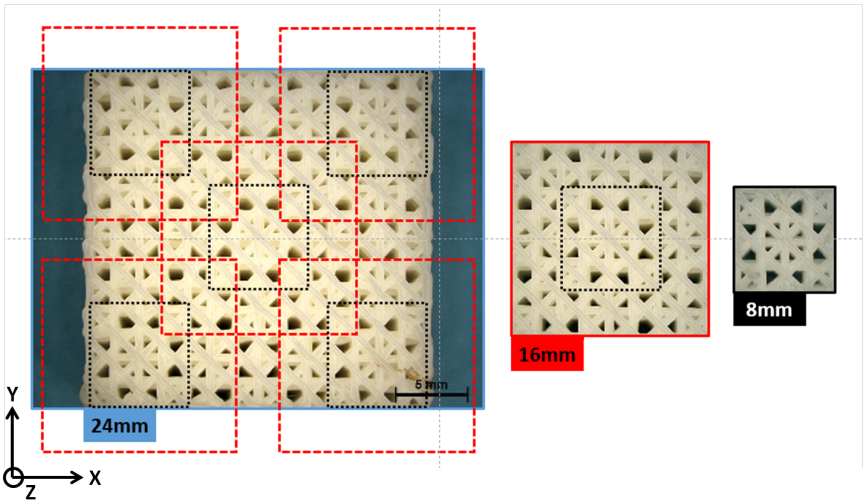

(a)

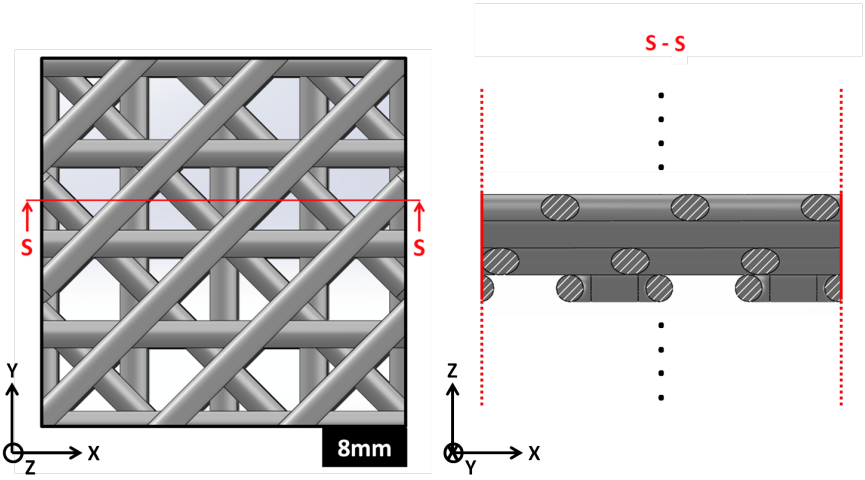

(b)

Figure 6: Morphological analyses of the cellular structures. (a) Top view (X-Y) of the cube-shaped structures with side 24, 16 and 8 mm. The morphological repeating patterns of the smaller structures are detected in the larger ones (C_8 in C_{16}, C_8 and C_{16} in C_{24}) and highlighted by means of dashed lines of the corresponding colour. (b) Top view (X-Y) of the CAD 3D model of the C_8 structure, accompanied by the cross section (X-Z) of a single 4-layer basic unit, **S - S**.

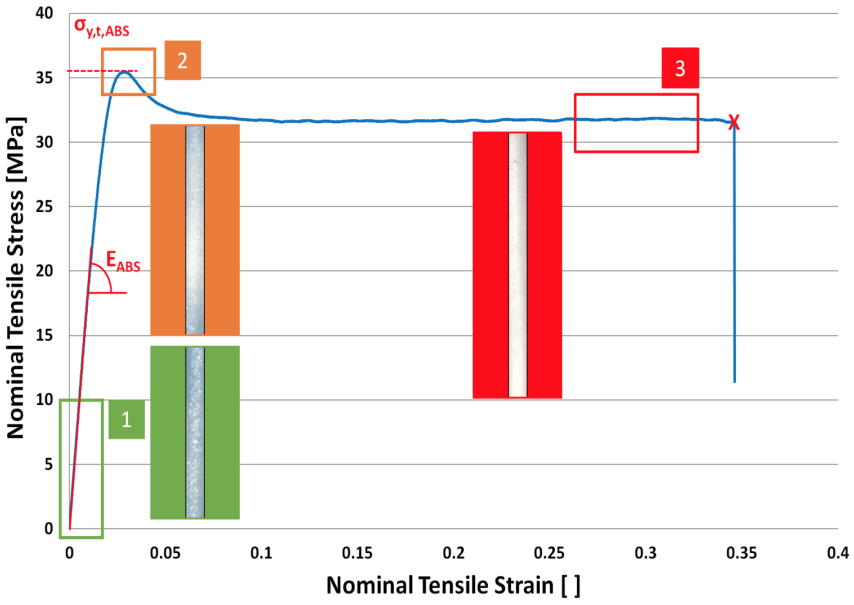

Figure 7: Nominal Tensile Stress vs Nominal Tensile Strain of the extruded ABS filament, accompanied by pictures of the specimen taken during the test.

The apparent stress, σ_{app}, vs apparent strain, ε_{app}, curves obtained from the monotonic compression tests carried out on the 3D-specimens are presented in Figure 8. The σ_{app}-ε_{app} curves of specimens loaded along the layer stacking direction show a characteristic trend, irrespective of the type of 3D-specimen examined. The curves can be described using a tri-linear model, with three distinct regions (I, II and III) and the slope in region II smaller than the other two (Figure 8a). Between adjacent regions, the curve shows a knee, which is broader in the region II-III. The comparison of the four σ_{app}-ε_{app} curves obtained from the C_{16} specimens loaded along the Z direction (Figure 8b) provides an indication of the high repeatability degree of the results . This whole trend, up to test interruption, might be interpreted on the basis of the behaviour of an elastic-plastic cellular solid under compression presented by (Gibson and Ashby, 1997). The three different regions would correspond to: the linear-elasticity region at low strain levels (region I); the structure plastic collapse zone (region

II); the structure densification zone (region III). The actual confirmation that this interpretation could be appropriate also for the 3D-structures here examined, when loaded along the 3D-growth direction, was given by the results got from i) the compression cyclic tests (Figure 8c), and ii) the observation of the structures deformed at large strain levels (Figure 9). Indeed, for the cyclic tests (Figure 5b), the $\varepsilon_{app,max,appl}$ applied to the specimen is assumed to be the sum of only two strain contributions: (i) a recoverable and (ii) a residual contribution (indicated with $\varepsilon_{app,res}$). The latter is "stored" in the specimen and, due to the mainly elastic-plastic response of the constituent material (ABS), can be directly related to plasticity. In general, the $\varepsilon_{app,res}$ data cannot be considered completely independent from the specific strain history applied during the experiment. Nevertheless, considering the specific scope of these experiments within the work, its influence on the outcomes can be assumed as negligible. The apparent residual deformation, represented as a function of $\varepsilon_{app,max,appl}$ in Figure 8c, shows that irrespective of the size, the 3D-structures start accumulating residual strain at deformation levels (between 3% and 5%) just smaller than the region of the I-II knee in the σ_{app}-ε_{app} curves. This indicates that this knee can be therefore associated with the plastic failure of the specimen. The absence of any residual strain contribution at the very beginning of the region I, at low strains, confirmed that the mechanical response could be considered as linear-elastic within this specific zone. In consideration of these outcomes, by resorting to a bi-linear representation of the curve around the I-II knee (see Figure 8a), a stress value representative of the plastic failure of the structure ($\sigma_{app,failure}$) and an apparent elastic modulus of the structure (E_{app}) were determined and taken as indexes of the mechanical strength and stiffness of the structure loaded along the Z direction, respectively. Their values are reported in Table 1. It is worth noting that the viscoelastic character of the constituent material is inherently set aside, giving it only a secondary role in the mechanical response of the structure.

Figure 9 shows the internal sectional views of the C_{16} structure after deformation under compression along the Z direction at strain levels of 0%, 20%, 40%

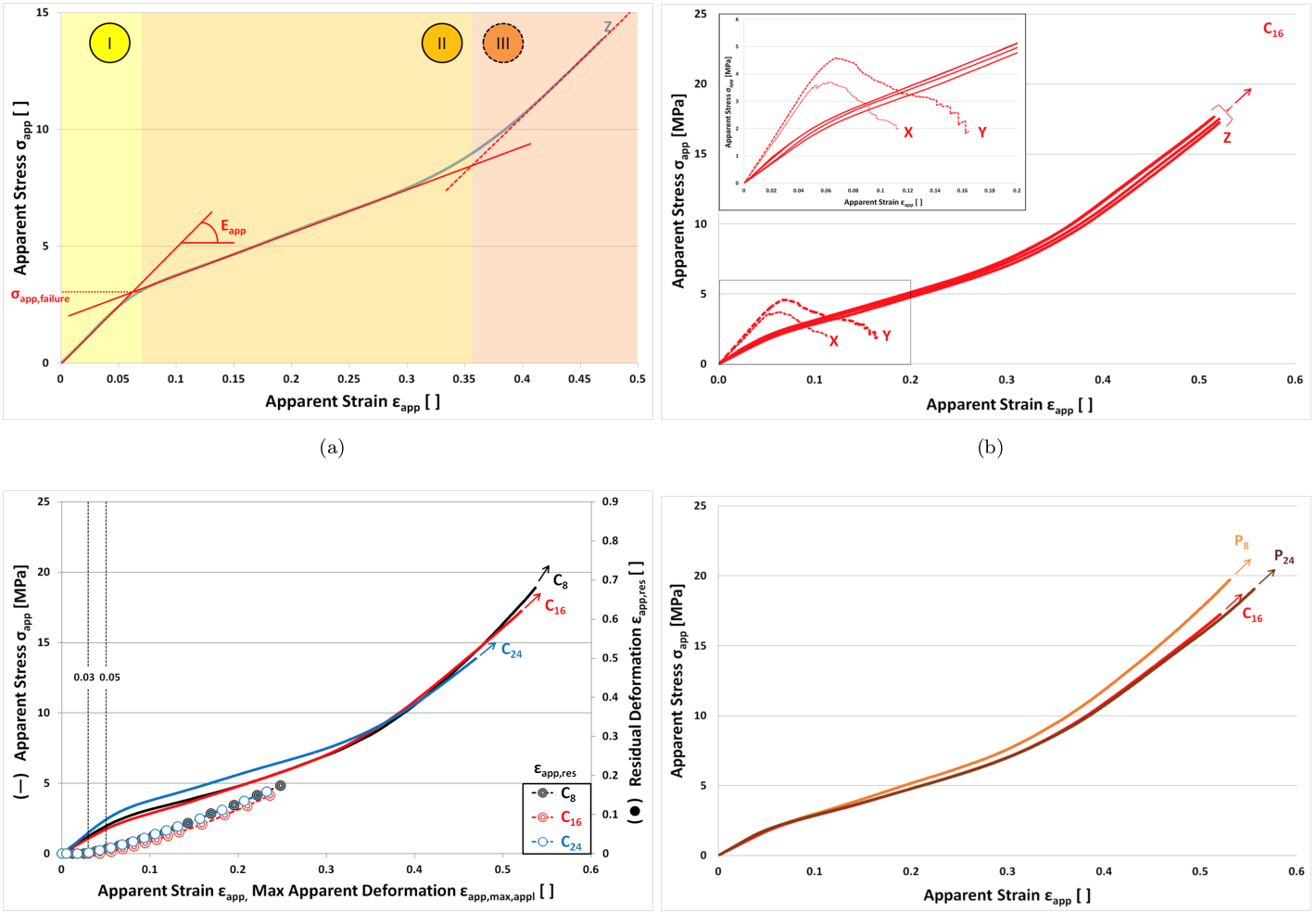

Figure 8: Compression tests on 3D printed cellular structures: output Apparent Stress, σ_{app}, vs Apparent Strain curve, ε_{app}. (a) Response of the cellular structures tested in Z (from a C_{24} specimen) and interpretation according to the tri-linear model (see text) proposed by (Gibson and Ashby, 1997). (b) Effect of testing direction (X, Y, Z), from tests carried out on C_{16} specimens. (c) Effect of size of cube-shaped specimens (C_8, C_{16}, C_{24}) on the mechanical response of the systems in layer stacking direction, Z (–). In addition, the final results of compression cyclic tests, expressed in terms of Residual Deformation $\varepsilon_{app,res}$, vs Max Apparent Deformation applied, $\varepsilon_{app,max,appl}$, is reported (●). The region where residual deformation starts to accumulate is indicated by black dashed lines. (d) Effect of height in specimens (P_8, C_{16}, P_{24}) characterized by the same square base side length (16 mm), on the mechanical response of the systems in Z. Tests in Z are interrupted at about 50% apparent strain.

and 60%, and subsequent cryogenic fracture. They provide information about the deformation mechanisms associated with region II and III of the σ_{app}-ε_{app} curve. A similar approach was adopted by (Wang et al., 2023). The direct relationship between the structural details emerging from the image corresponding to the undeformed structure and the sectional view of the CAD model reported in Figure 6b clearly comes out. Assuming the four specimens nominally identical, the results in the different photos can be considered as consecutive frames of a unique progressive deformation process. By comparing the undeformed structure with that obtained at 20% strain, it can be observed that the structure collapses homogeneously at a macro-scale, via shape distortion and size reduction of the framed spaces defined by the ABS filament. Interestingly, whitened zones appear. Considering that ABS extruded filament whitening (Figure 7) is associated to voiding - a volumetric deformation mechanism under tension - it follows that the ABS walls in the 3D structure undergo local tensile stresses equal to $\sigma_{y,t,ABS}$ (36.2 ± 2.6 MPa). This value is about seven times higher than the corresponding apparent stress resisted by the structure under compression at 20% strain (Figure 8b), and this confirms the high degree of complexity of the state of stress undergone at large strains by the material that forms a cellular solid (Gibson and Ashby, 1997). Figure 9 clearly shows that by increasing the level of applied deformation, the extent of shape distortion and cell size reduction increases giving rise to an evident densification of the structure. The whitened zones increase in number and area extension, and tend to concentrate along Z-oriented lines at the filament contact points between the stacking layers (see the image of the 40% deformed structure). The structures deformed at apparent strain levels of 20%, 40% and 60% exhibited non-recoverable strain levels of 9.6%, 29.2% and 51.3%, respectively. By comparing the data of $\rho_{rel,3D}$ measured on the deformed structures with those taken in the undeformed state, an increase in apparent density values of 7%, 29% and 54%, respectively, emerged. Interestingly, this outcome indicates the occurrence of densification already at an applied strain of 20%, which is right in the middle of the region II of the σ_{app}-ε_{app} curve (see Figure 8a). Therefore, this specific region, initially associ-

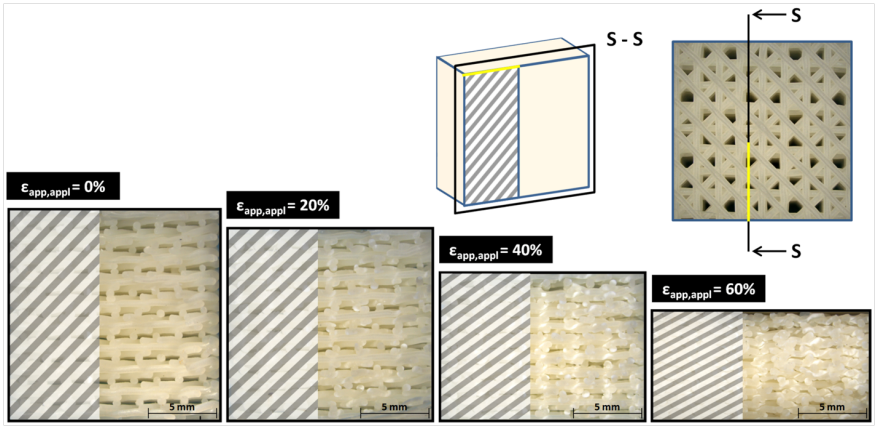

Figure 9: Optical microscope pictures of the **S - S** cross sections (from cryogenic fracture in liquid nitrogen) from 4 C_{16} specimens tested at different levels of $\varepsilon_{app,max,appl}$ (0%, 20%, 40%, 60%). The sharp notch, introduced in the specimens (in the same position showed in Figure 6b) after testing, is indicated in yellow. The portion of specimen containing the notch is overshadowed using grey stripes pattern.

ated only to the structure plastic collapse, has to be related also to structure densification. In agreement with (Egan et al., 2022), who worked on 3D-printed polymeric systems with 0°, 45°, 90°, −45° orientations and with relative density similar to that of the structures here examined, the occurrence of structure densification in the region II is probably at the basis of the slope exhibited by the σ_{app}-ε_{app} curve in this specific region (largely higher than that expected for an ideal elastic-plastic behaviour, which is ≈ 0). By comparing the response (stress-strain curve) exhibited by the structures examined with that showed by other elastic-plastic cellular solids within the region II, it emerges that such a smooth trend (completely free of stress oscillations) seems to be typical of structures where struts in Z-direction are either not present (Shalchy et al., 2020) (Bachtiar et al., 2021) or characterized by low slenderness. On the contrary, when such high-slenderness struts are present, a scattering trend with repeated peaks is typically observed (Eren et al., 2022) (Wang et al., 2023), which can be attributed to their local buckling.

Regarding the specimen size effects, the σ_{app}-ε_{app} curves of the cube-shaped

specimens with different sizes (C_8, C_{16}, C_{24}) loaded along the Z direction (Figure 8c) show a very similar response for C_8 and C_{16} specimens, whereas C_{24} presents slightly higher stresses in both region I and II. Therefore, C_{24} has slightly higher values of E_{app} and $\sigma_{app,failure}$, with respect to C_8 and C_{16} (see Table 1). The response of the prism-shaped specimens having the same square base of C_{16} but different heights (P_8 and P_{24}) - Figure 8d and Table 1 - suggests that the higher values of E_{app} and $\sigma_{app,failure}$ measured for C_{24} are related to its two-dimensional development on the X-Y plane rather than to its height. Indeed P_{24}, with same base of C_{16} and same height of C_{24}, exhibits the same stiffness of C_{16}, and even a smaller strength. The way the five different C_{16} structures (Figure 6a) combines to form the C_{24} specimen might be responsible of a synergistic effect that promotes the increase in the mechanical properties observed for C_{24}. Regarding the effect of the loading direction(Figure 8b), the compression response along a direction orthogonal to Z (either X or Y) shows a σ_{app}-ε_{app} curve very different from the tri-linear trend observed for compression along the Z direction. This peculiar trend is characterized by the achievement of a peak in the stress associated to the onset of delamination phenomena between two adjacent layers, originating from the weakest points of the structure. The progress of the delamination phenomena, even accompanied by buckling, explains the irregular stress decrease observed beyond the stress peak. The stress at the peak was taken as $\sigma_{app,failure}$ and, from the linear region of curve at very low strains, the value of E_{app} was determined (Table 1). As expected, given the geometrical symmetry of the structure, no difference was observed between the values of E_{app} and $\sigma_{app,failure}$ measured along X or Y. When loaded along a direction that is orthogonal to the layer stacking one, the structure is ≈ 1.8 times stiffer and ≈ 2 times stronger than along Z (from a forced relation between strength data associated to two different failure mechanisms).

Following the approach typically used in literature for cellular solids (Gibson and Ashby, 1997) the values of E_{app} and $\sigma_{app,failure}$, normalized over the elastic modulus and yield stress of the constituent material, E_{ABS} and $\sigma_{y,t,ABS}$, respectively, are plotted against the relative density, $\rho_{rel,3D}$ (Figure 10a and 10b,

respectively). One data-point corresponds to one specimen; the data-points corresponding to the two C_8 specimens having $\rho_{rel,3D}$ outside 0.35 ± 0.02 (see section 3.1) are also indicated. For both E_{app} and $\sigma_{app,failure}$, the data coming from the X and Y loading directions are visibly above those measured along the Z direction. The two series of data in the density region of interest are very well grouped, especially in the stiffness plot, and the data-points coming from the specimens with different sizes or heights mix well with each other. By referring to the data measured under compression along the Z direction, only the variation of $\rho_{rel,3D}$ can induce an appreciable effect on the mechanical properties of the 3D-structure in agreement with the cellular material analysis approach (Gibson and Ashby, 1997) described by a power law curve:

$$y = d \cdot x^f \tag{2}$$

In Figure 10a, which refers to the stiffness, such a curve was traced imposing $d = 1$ and taking f as the mean of the f-values obtained by forcing this expression to each single Z direction data-point, including also those coming from the two C_8 specimens with $\rho_{rel,3D}$ outside the region limited by the dot lines (the mean f-value resulted equal to 3.63). In Figure 10b, which refers to the strength, such a curve was traced according to the theoretical relationship proposed for the plastic-collapse strength of open-celled foams (with d and f equal to 0.3 and 3/2, respectively); it intercepts the group of experimental Z-direction data-points. The extent to which the constituent polymer (ABS) contributes to the 3D-structure stiffness is smaller with respect to that to which it contributes to the 3D-structure strength, in agreement with what observed by the authors for a very different 3D-structure manufactured by FDM (based on a different polymer, with a different architecture and much denser) (Pagano et al., 2021).

4. Conclusions

In this work, ductile polymer (ABS) model structures were manufactured by FDM, and their mechanical behaviour investigated under compression. The

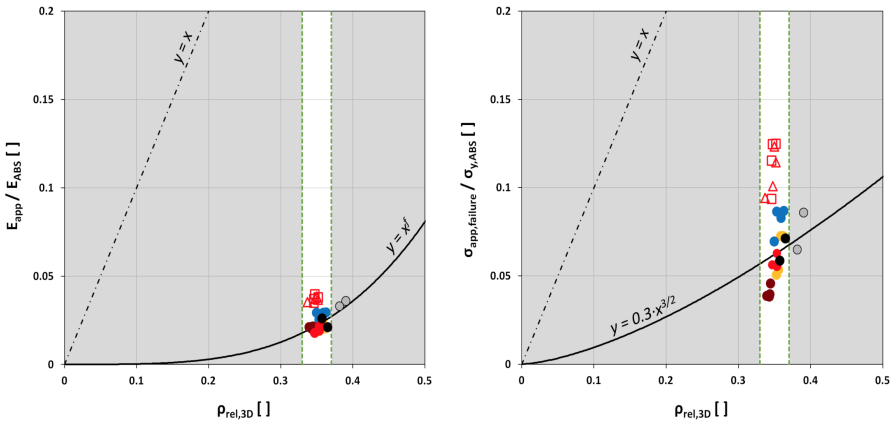

(a) (b)

Figure 10: (a) Relative stiffness, E_{app}/E_{ABS}, and (b) relative strength, $\sigma_{app,failure}/\sigma_{y,ABS}$, as a function of the relative density, $\rho_{rel,3D}$, of the 3D-structures. Full circles: data-points from tests carried out with the loading direction parallel to the layer stacking direction (**black**, C_8; **red**, C_{16}; **blue**, C_{24}; **orange**, P_8; **brown**, P_{24}; grey circles refer to C_8 specimens with $\rho_{rel,3D}$ outside 0.35 ± 0.02). **Red** open symbols: data-points from tests carried out with the loading direction orthogonal to the layer stacking direction (triangles, $C_{16\text{-}X}$; squares, $C_{16\text{-}Y}$). Continuous line is the power law curve traced according to Eq. 2 by using d = 1 and f = 3.63 in (a) and d = 0.3 and f = 3/2 in (b) (see text). Vertical dashed lines traced at $\rho_{rel,3D} = 0.33$ and at $\rho_{rel,3D} = 0.37$.

peculiar structure design strategy adopted led to obtain three-dimensional open-celled systems (with a porosity degree of 65%), composed of unit cells with different shapes and dimensions assembled in such a way to form regularly repeating patterns. Effects of the test specimen size, height and loading direction were investigated, and the results analyzed in the light of the outcomes from cyclic compression experiments and morphological analyses of the cryogenic fracture surfaces of specimens compressed at high strain levels. A markedly non-isotropic response was observed. The compressive behavior in the layer stacking direction was traced back to the elastic-plastic case, with the stress-strain curve exhibiting three different regions: a linear-elasticity region at low strain levels (region I); a region where the structure plastic collapse occurs, combined with the initiation of the structure densification (region II); a structure densification region (region III). The size effects is not dominant, but observable on the specimens with the largest size examined, which showed slightly higher levels of stiffness and strength. This is tentatively attributed to their peculiar structure, resulting from a complex interconnection of the basic structures forming the smaller specimens, which are arranged in co-shared regions and with connecting zones being created. Taking into account the mechanical response of the constituent material (characterized in the form of the extruded filament, under tension), the fundamental role of the architecture on the mechanical response of the 3D-structures is definitely evident.

The outcomes of the present paper form the basis for a subsequent work (already in progress) on the study of the structural integrity of the 3D-structure here examined, under the framework of the fracture mechanics.

5. Acknowledgments

The authors are grateful to Fabbrica d'Armi Pietro Beretta S.p.A. (Gardone Val Trompia, Brescia, Italy), Industrie Polieco-M.P.B. S.r.l. (Cazzago San Martino, Brescia, Italy) and Bioteck S.p.A. (Arcugnano, Vicenza, Italy) for the support kindly provided. A special thanks to Michelangelo Conter, student at

University of Brescia, Italy, for the CAD models.

6. Funding

Financed by the European Union - NextGenerationEU (National Sustainable Mobility Center CN00000023, Italian Ministry of University and Research Decree n. 1033 - 17/06/2022, Spoke 11 - Innovative Materials & Lightweighting). The opinions expressed are those of the authors only and should not be considered as representative of the European Union or the European Commission's official position. Neither the European Union nor the European Commission can be held responsible for them [CUP: D83C22000690001].

References

Abou-ali, A.M., Al-ketan, O., 2019. Mechanical Response of 3D Printed Bending-Dominated Ligament-Based Triply Periodic Cellular Polymeric Solids. Journal of Materials Engineering and Performance 28, 2316–2326. doi:10.1007/s11665-019-03982-8.

Agnelli, S., Baldi, F., Castellani, L., Pisoni, K., Vighi, M., Laiarinandrasana, L., 2018. Study of the plastic deformation behaviour of ductile polymers: Use of the material key curves. Mechanics of Materials 117, 105–115. doi:10.1016/j.mechmat.2017.11.002.

Askari, M., Hutchins, D.A., Thomas, P.J., Astolfi, L., Watson, R.L., Abdi, M., Ricci, M., Laureti, S., Nie, L., Freear, S., Wildman, R., Tuck, C., Clarke, M., Woods, E., Clare, A.T., 2020. Additive manufacturing of metamaterials: A review. Additive Manufacturing 36, 101562. doi:10.1016/j.addma.2020.101562.

Bachtiar, E.O., Ritter, V.C., Gall, K., 2021. Structure-property relationships in 3D-printed poly (L-lactide-co-ϵ-caprolactone) degradable polymer. Journal of the Mechanical Behavior of Biomedical Materials 121. doi:10.1016/j.jmbbm.2021.104650.

Egan, P.F., Khatri, N.R., Parab, M.A., Arefin, A.M.E., 2022. Mechanics of 3D-Printed Polymer Lattices with Varied Design and Processing Strategies. Polymers 14, 5515. doi:10.3390/polym14245515.

Eren, O., Sezer, H.K., Yalcin, N., 2022. Effect of lattice design on mechanical response of PolyJet additively manufactured cellular structures. Journal of Manufacturing Processes 75, 1175–1188. doi:10.1016/j.jmapro.2022.01.063.

Gibson, L.J., Ashby, M.F., 1997. Cellular solids: Structure and properties, second edition. Cambridge University Press. doi:10.1017/CBO9781139878326.

Javaid, M., Haleem, A., 2018. Additive manufacturing applications in medical cases: A literature based review. Alexandria Journal of Medicine 54, 411–422. doi:10.1016/j.ajme.2017.09.003.

Kumar, A., Kumar, A., Pandey, A., Sahu, S., Kumar, N., Singh, R.P., 2022. Analysing the compressive behaviour of different PLA scaffolds fabricated through FFF process. Advances in Materials and Processing Technologies 00, 1–14. URL: https://doi.org/10.1080/2374068X.2022.2093005, doi:10.1080/2374068X.2022.2093005.

Ling, C., Cernicchi, A., Gilchrist, M.D., Cardiff, P., 2019. Mechanical behaviour of additively-manufactured polymeric octet-truss lattice structures under quasi-static and dynamic compressive loading. Materials & Design 162, 106–118. doi:10.1016/j.matdes.2018.11.035.

Macosko, C.W., 1994. RHEOLOGY Principles, Measurements and Applications. Wiley-VCH.

Maskery, I., Sturm, L., Aremu, A.O., Panesar, A., Williams, C.B., Tuck, C.J., Wildman, R.D., Ashcroft, I.A., Hague, R.J.M., 2018. Insights into the mechanical properties of several triply periodic minimal surface lattice structures made by polymer additive manufacturing. Polymer 152,

62–71. URL: https://doi.org/10.1016/j.polymer.2017.11.049, doi:10.1016/j.polymer.2017.11.049.

Pagano, C., Rebaioli, L., Baldi, F., Fassi, I., Pagano, C., Rebaioli, L., Baldi, F., Fassi, I., 2021. Relationships between size and mechanical properties of scaffold-like structures. Mechanics of Advanced Materials and Structures 28, 1812–1817. doi:10.1080/15376494.2019.1709675.

Penumakala, P.K., Santo, J., Thomas, A., 2020. A critical review on the fused deposition modeling of thermoplastic polymer composites. Composites Part B: Engineering 201, 108336. doi:10.1016/j.compositesb.2020.108336.

Platek, P., Rajkowski, K., Cieplak, K., Sarzynski, M., Malachowski, J., Wozniak, R., Janiszewski, J., 2020. Deformation Process of 3D Printed Structures Made from Flexible Material with Different Values of Relative Density. Polymers 12, 2120. doi:10.3390/polym12092120.

Shalchy, F., Lovell, C., Bhaskar, A., 2020. Hierarchical porosity in additively manufactured bioengineering scaffolds: Fabrication & characterisation. Journal of the Mechanical Behavior of Biomedical Materials 110, 103968. doi:10.1016/j.jmbbm.2020.103968.

Wang, X., Gao, T., Shi, C., Zhou, Y., Li, Z., Wang, Z., 2023. Effect of geometric configuration on compression behavior of 3D-printed polymeric triply periodic minimal surface sheets. Mechanics of Advanced Materials and Structures 30, 2304–2314.

Zhou, C., Yang, K., Wang, K., Pei, X., Dong, Z., Hong, Y., Zhang, X., 2016. Combination of fused deposition modeling and gas foaming technique to fabricated hierarchical macro / microporous polymer scaffolds. Materials and Design 109, 415–424. doi:10.1016/j.matdes.2016.07.094.